J Mater Sci: Mater Electron (2023) 34:1443

Development of cupric sulphate nanocrystals on fluorine-doped tin oxide substrates using hydrothermal technique

Chinedu Christian Ahia[1,*] and Edson L. Meyer[1]

[1] *Institute of Technology, University of Fort Hare, Private Bag X1314, Alice 5700, South Africa*

Received: 13 April 2023
Accepted: 14 June 2023
Published online: 29 June 2023

ABSTRACT

Cupric sulphate nanocrystals (NCs) are desirable for a number of applications. The NCs were grown using a hydrothermal technique on Fluorine-doped Tin Oxide substrate which was sandwiched into the grooves of a sample holder at an angle between 45° and 90° relative to the wall of a 100 ml Teflon container. The surface features were observed using an optical microscope while atomic scale features which are not visible under the optical microscope were investigated using a scanning electron microscope and atomic force microscope. Details of the weight percentage composition were investigated on the sample by means of energy-dispersive X-ray spectroscopy. A broad absorption spectrum from 690 to 1100 nm, having a full width at half maximum value of 254 nm and an energy excitonic absorption peak in the visible region at 810 nm, was observed when the NCs are dissolved in water (hydrate solution) contrary to the highest absorption peak which was observed at 678 nm for the anhydrous compound. A total number of 16 vibrational frequencies were observed from Raman scattering while five active modes were visible in the Fourier Transform Infrared spectrum. Information on room-temperature photoluminescence and fluorescence spectroscopy measurements obtained from the NCs is reported. The deposition technique adopted in present work could be optimized for the high-yield production of more uniform layers of ultrathin nanostructures with increased aptitude for various applications.

1 Introduction

Numerous metallic nanoparticles have attracted recent interest and are presently explored for prospective utilization as a cheap substitute for high-cost metal nanoparticles in the micro-electronics sector. The effective harnessing of the optical properties of materials in recent times has prompted a surge in the development of different optoelectronic devices for various applications such as sensors, lasers and light-emitting diodes (LEDs). Copper is a noble metal which is renowned for its high thermal

Address correspondence to E-mail: achinedu@ufh.ac.za

https://doi.org/10.1007/s10854-023-10839-3

and electrical conductivity. It also has good alloying potentials, malleable and resistant to corrosion. Metallic copper can react with sulphur at high temperature to yield copper sulphide which oxidizes to produce copper sulphate. Copper (II) sulphate ($CuSO_4$) is an inorganic compound with numerous applications such as in agriculture, medicine and industry. It also serves as a major constituent of the electrodes and electrolytes in batteries. $CuSO_4$ usually absorbs moisture from the atmosphere to form a more stable compound called pentahydrate ($CuSO_4{\cdot}5H_2O$). However, $CuSO_4$ is amorphous, while $CuSO_4{\cdot}5H_2O$ is crystalline.

The effect of solution cooling rate and incorporation of sodium chloride on the crystal size distribution, growth rates, morphology and configuration of copper sulphate pentahydrate crystals has been reported [1], with the aim of estimating the result on crystal structure, of utilizing salt water as an substitute to pure water. Currently, a considerable number of chemical techniques have been developed for the synthesis of cupric sulphate. For instance, slow evaporation technique has been reported by different authors for the synthesis of cupric sulphate crystals [2, 3]. Similarly, a technique for developing large single crystals of $CuSO_4{\cdot}5H_2O$ for application as broadband UV optical filters has been investigated [4]. Furthermore, a method of investigating the optical and structural properties of triclinic crystals has been reported during a dispersion analysis which was implemented on a $CuSO_4{\cdot}5H_2O$ single crystal. During the analysis, the spectra of polycrystalline $CuSO_4{\cdot}5H_2O$ was modelled using established oscillator parameters and the equivalent dielectric function tensor [5]. Other studies on $CuSO_4{\cdot}5H_2O$ that has been reported include its magnetic field dependence of specific heat [6], indirect nuclear spin–spin interaction in $CuSO_4{\cdot}5H_2O$ [7], and torsion-effusion studies on thermal decomposition of $CuSO_4$ [8]

The utilization of FTO as substrate in material deposition has gained momentum due to its inert disposition to a wide range of chemicals. Results on distinctive cyclic voltammetry of FTO substrate measured in 0.25 M $CoSO_4$ + 0.005 M $CuSO_4$ solutions have been reported during an investigation of the electrochemical and structural characteristics of cobalt–copper electrodeposits [9]. Some instances include the use of nebulized spray pyrolysis techniques for the development of Cu-doped ZnS and Al-doped ZnS thin films on FTO substrate [10], and the use of two-step electrodeposition method for the fabrication of $Cu_2O/g\text{-}C_3N_4$ heterojunction film on an FTO substrate [11]. The characterization of copper sulphates using Raman spectroscopy has been reported to be challenging due to the colour spectrum of the compound [12]. The authors [12] also suggested that the application of a diode laser operating at 785 nm excitation permits improved band separation in the low-wavenumber region but cannot be used to observe vibrational frequencies at the high wavenumber region. The aforementioned challenge was mitigated in this study by acquiring the Raman spectrum from the cupric sulphate using a fast imaging ultra-high-throughput spectrometer (UHTS 400) with a solid-state laser of wavelength 532 nm, which permits the investigation of vibrational frequencies within the high wavenumber domain.

The successful fabrication of ultrathin nanostructures with good structural integrity through hydrothermal deposition require a high degree of stoichiometric knowledge of the compound and the precise manipulation of the thermodynamic processes involved including factors such as the interaction between crystal nuclei, diffusion and sticking coefficients, PH value, and molarity of the reagents. To date, numerous ultrathin metal sulphide nanostructures have been synthesized using various techniques. However, there is limited literature reporting a detailed investigation on the structural and optical properties of hydrothermally deposited cupric sulphate NCs on FTO. In present work, FTO was chosen as a desirable substrate due to its susceptibility for application in different areas of device fabrication technology which includes electrodeposition, solar cell's window layer, transparent contact in optoelectronics devices, and gas sensor devices amongst many others. The results contained in the present study can be useful towards the advancement of innovative procedures for controlling the quality of crystal deposition with the aim of enhancing their structural integrity and optical properties.

2 Experiment

The reagents used in this work were of analytical grade and hence used without the need for further purification. The Copper (II) oxide (ACS reagent, ≥ 99.0%) and Sulphuric acid (H_2SO_4, 98% conc.) utilized in the synthesis were obtained from Sigma-

Aldrich, while the FTO substrates were supplied by Techinstro. The FTO substrates were sequentially degreased in warm trichloro-ethylene and then rinsed in acetone twice before immersion in methanol. This procedure was repeated twice for approximately 180 s before final rinsing in deionized water and blown dry with nitrogen. The degreased substrate was sandwiched into the grooves of a sample holder at an angle between 45° and 90° relative to the wall of a 100 ml Teflon container such that the active side was facing upwards as shown in Fig. 1C and D. A 55 ml solution of CuO that has been dissolved in dilute H_2SO_4 at constant magnetic stirring for 15 min to form a homogeneous mixture was then poured into the container and properly sealed with its cover as a precaution to prevent water evaporation. The Teflon container is subsequently inserted in a stainless-steel autoclave reactor and placed inside an oven that has been preheated to approximately 100 °C for 45 min. This phase was successively followed by immersing the autoclave in a water bath for approximately 25 min and allowed to cool to room temperature. After cooling, the sample was removed from the Teflon container, rinsed in deionized water, and dried with nitrogen. The entire procedure prior to placing the autoclave in a preheated oven was conducted in an organic fume hood.

Optical micrographs of the sample and FTO substrate were acquired using a Zeiss EC "Epiplan" DIC objective with × 20 magnification, a numerical aperture of 0.4, and a working distance of 7 mm. FL emission spectrum from the sample was measured with the aid of a PerkinElmer LS 45 Luminescence spectrometer fitted with Xenon discharge lamp source, while room-temperature PL measurements were conducted on the sample using a Mini PL 110 detection system with a pulsed deep UV laser excitation wavelength of 248.6 nm (5.0 eV). The functional groups present in the sample were investigated using a PerkinElmer Spectrum Two Fourier Transform Infrared (FT-IR) Spectrometer which is fortified with a mid-infrared detector and a diamond crystal Universal Attenuated Total Reflectance (UATR) sampling accessory that has a reduced sensitivity in the approximate range 1900–2700 cm^{-1}. Likewise, a Bruker Vertex 80v spectrometer and a PerkinElmer Lambda 365 Double Beam UV–Visible Spectrophotometer with UV Express software were simultaneously used to establish the UV–VIS characteristics of the nanocrystals. SEM micrographs showing the crystal structure and distribution were obtained from the Tescan MIRA3 SEM which is equipped with a retractable backscatter detector, while EDX was carried out on the Nova NanoSEM, using an oxford

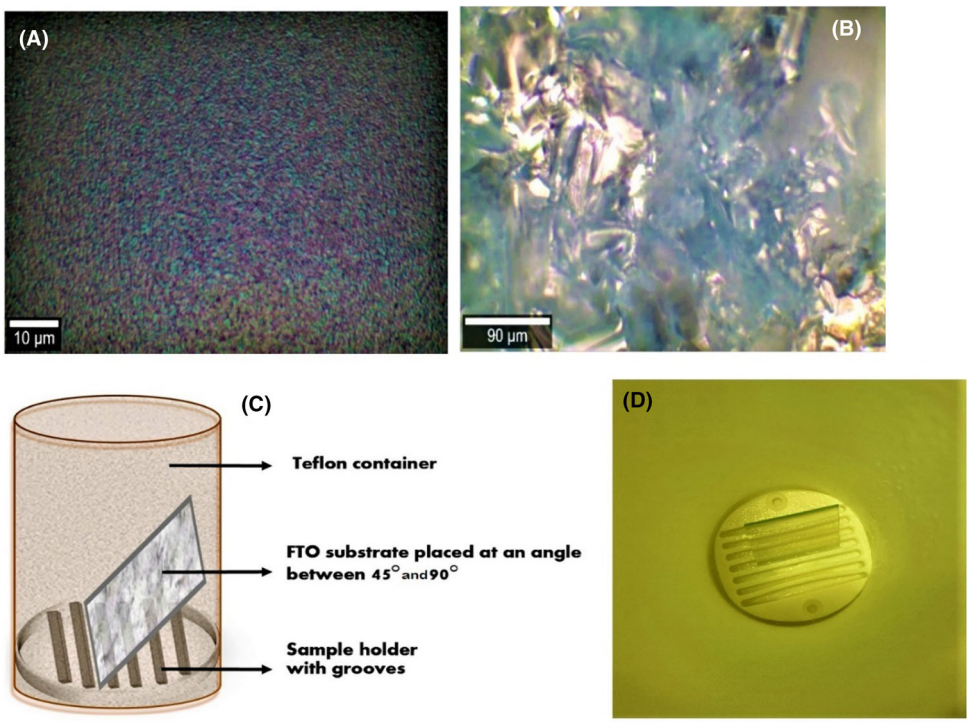

Fig. 1 Optical micrographs showing **A** FTO substrate before deposition and **B** After deposition of $CuSO_4$ NCs **C** Side-view schematic representation showing FTO substrate placed at an angle in the Teflon container **D** Top-view photographic image of FTO substrate described in (c)

X-Max detector and INCA software. The EDX analysis was collected at 20 kV, and a spot size of 0.38 nA for 20 s.

Finally, room-temperature Raman signal from the sample was acquired using a WiTec alpha 300RA + confocal Raman microscope furnished with optimized UHTS spectrometers, a frequency-doubled Nd:YAG 532 nm excitation laser wavelength high-throughput configuration and motorized scanning stage, while the surface morphology of the sample was investigated using a Bruker Dimension FastScan scanning probe microscope (SPM) which was mounted on an integrated air table with the sample stage been enclosed in a high-performance acoustic hood (AVH-1000) in order to provide increased acoustic and vibration isolation.

3 Results and discussion

Figure 1A displays the surface features of the FTO substrate before deposition as observed from the optical microscope. A close observation indicates that the substrate surface is not typically smooth but rather characterized with some degree of roughness while Fig. 1B shows the presence of a fairly thick non-uniform layer deposition. A schematic image which depicts the side view of the Teflon container with the FTO substrate immersed inside the groove of the sample holder, while the FTO side is facing upwards is displayed in Fig. 1C. Figure 1D is the top-view photographic image of the FTO substrate inclined at an angle with the wall of the Teflon container. To examine atomic scale features which are not visible under the optical microscope, AFM analysis was carried out on the sample. Further investigation of the layer in Fig. 1B using AFM (tapping mode condition) suggests a corrugated morphology consisting of densely populated nanocrystals as seen in Fig. 2A.

For high precision and sensitivity imaging in tapping mode, a BRUKER high-quality rectangular silicon AFM probe/cantilever (RTESPA) with resonance frequency (f_o) = 300 kHz, and spring constant (K) = 40 N/m was used during data acquisition. A slow scan axis function was enabled with a scan rate and sample line of 0.300 Hz and 256, respectively, for an image-projected surface area of 25.0 μm^2. Likewise, other scan parameters such as the drive amplitude, tip velocity, amplitude setpoint, and the tapping mode deflection limit were systematically adjusted to appropriate values to acquire optimal image resolution. To investigate the distribution of the deposited structure and precisely measure the size dimensions of the surface features in Fig. 2A and C, a line profile scan across the surface of the bare FTO substrate and the sample containing the synthesized crystals was carried out over a lateral distance of approximately 5 μm on the substrate and the sample, respectively. The preferential area on both the bare FTO substrate and on the sample where the line scan was executed was arbitrarily chosen based on knowledge of the scanned image dimensions as shown in Fig. 2B and C. Other parameters considered when choosing a preferential spot for line scan include the presence of unique morphological features and consistent trend in raster pattern. Contributions from the substrate roughness are taken into consideration as precision when analysing the actual size distribution of the deposited crystals. Data obtained from the line profile scan across the surface of the bare FTO substrate and the sample can be presented to display the relationship between surface roughness and lateral distance as shown in Fig. 2D. Results from the line scan give an average height of 65 nm, and a lateral size dimension in the range 90–450 nm which corresponds to a mean base length of 270 nm for the crystal-like structures, as determined from height profile measurements. A more comprehensive description of the scan parameters and conditions adopted in acquiring the AFM data can be found in the previous report [13]. The results obtained from AFM analysis of the sample revealed corrugated surface morphology with densely populated nanosized crystal-shaped particles as seen in Fig. 2A. AFM studies conducted on the as-grown sample show a high surface roughness value of 21 nm root-mean square (RMS) for a scan size of 5×5 μm^2, with a threshold height of $\sim$ 103 nm projecting from the surface. In a study [14] which involved a modelled tip-surface-sample interaction, the measured height of nanoscale structures using AFM was reported to consistently yield lower value than the accurate value, a phenomenon attributable to the effect of the local probe-sample geometry. To mitigate anomaly in measured values using AFM technique, the choice of scan parameters and AFM probes is fundamental for the effective sensing of trivial modifications in morphological properties of the samples. In present study, the

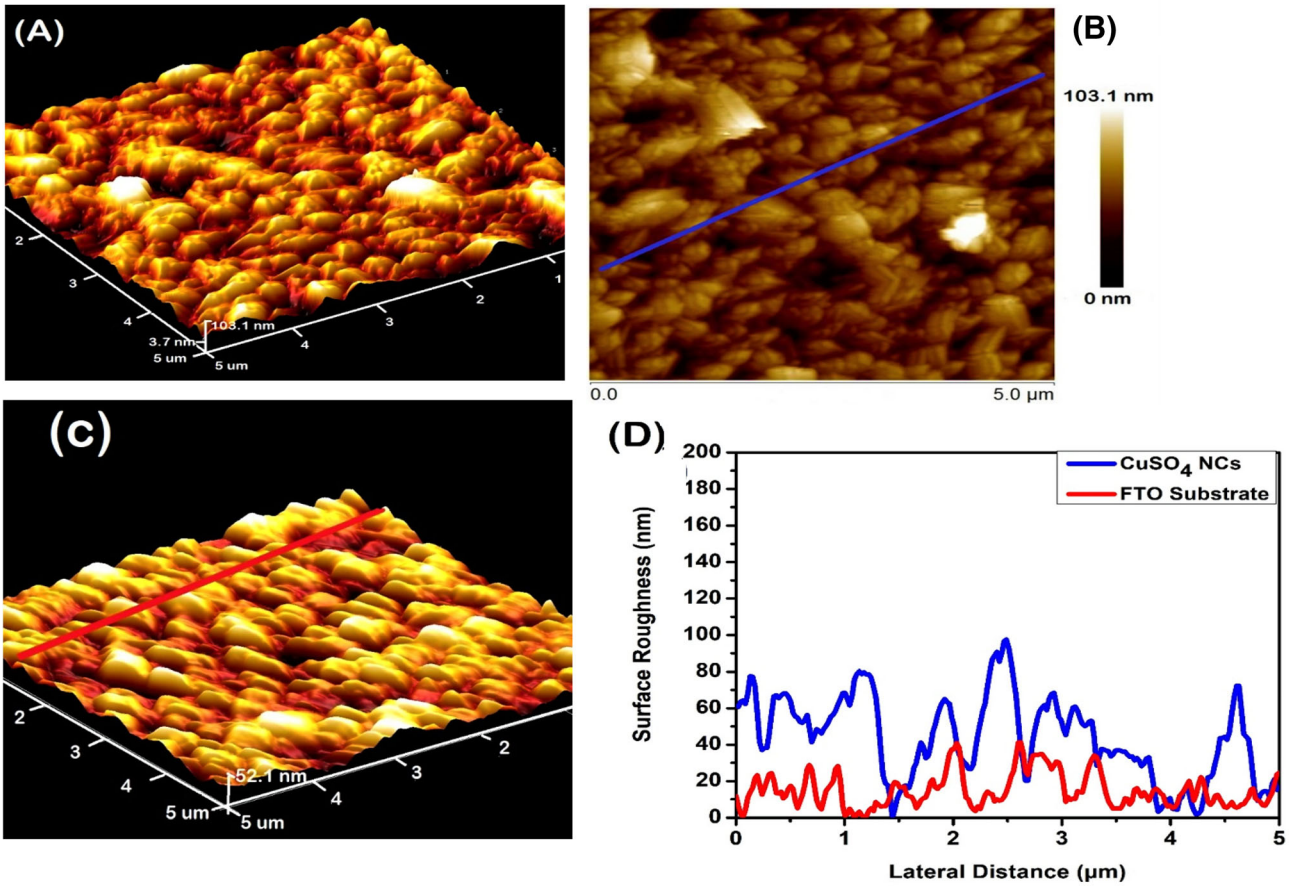

Fig. 2 **A** 3D AFM image displaying surface morphology of $CuSO_4$ NCs **B** 2D AFM image of $CuSO_4$ NCs indicating specific spot of line scan on the AFM image **C** 3D AFM image of bare FTO substrate showing spot of line scan on the micrograph **D** Corresponding line profiles across a section on both the sample and the FTO substrate, respectively

measured values obtained from the sample using AFM technique are in agreement with projections from SEM measurements.

The SEM images were acquired using an In-beam secondary electron detector which enables high-resolution imaging desired for comprehensive topographical characterization and hence, observation of both unique and conspicuous surface features present in a sample.

The SEM image in Fig. 3 shows dispersed clusters and coalesced nanocrystals which are non-uniformly distributed on the surface of the FTO substrate with high levels of agglomeration of the $CuSO_4$ particles resulting from adhesion. The increased agglomeration is suggested to induce a reduction in the surface-free energy of the sample which ultimately leads to increased crystallite size and concentrated surface area. The different size distribution of the crystals as observed from the SEM micrographs in Figs. 3 indicates the inconsistent growth rate of the crystals respectively. In general, non-uniformity in crystal growth rate/pattern can be triggered by a number of factors such as the presence of dislocation or incorporation of impurities, lattice strain, arbitrary surface adsorption, and deformation [15, 16].

The preferential region on the FTO which is depicted as pink square outlines in Fig. 4A is spots where the compositional information was extracted using direct analytical measurements by means of energy-dispersive X-ray spectroscopy (EDX). Several analytical measurements (spectrum 1 to 5) were carried out on the sample for precision. Figure 4B is the EDX spectrum containing compositional data acquired from a large surface area (spectrum 5) on the sample as shown in Fig. 4A. The EDX spectrum reveals the constituent elements in the sample while details of the weight percentage composition extracted from each spectrum spot (spectrum 1 to 5) on the

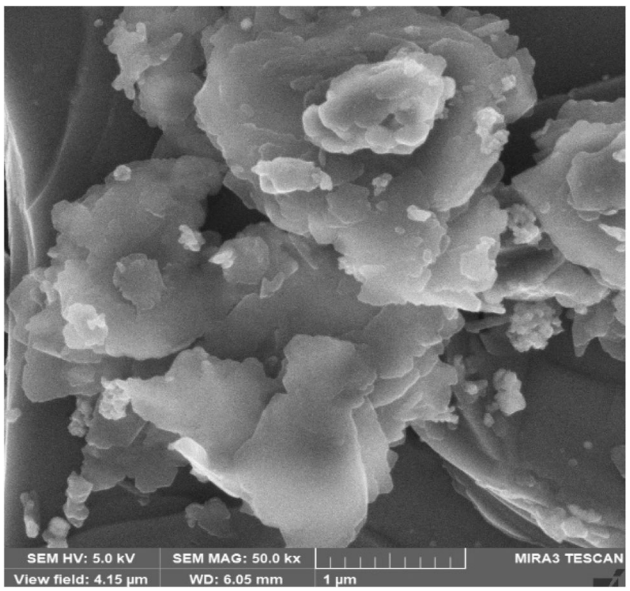

Fig. 3 Typical planar view of SEM micrograph showing structural measurements obtained from $CuSO_4$ NCs on FTO using different magnifications

sample as displayed in Fig. 4A are contained in Table 1.

The existence of carbon in the regions originates from the protective carbon layer deposited over the specimen surface to prevent curtaining artefacts during FIB preparation.

The PL spectrum in Fig. 5A was acquired at room temperature from the sample and revealed a broad emission line with peaks in the visible region. In the present study, all luminescence spectra were fitted after appropriate baseline subtraction using a deconvolution procedure in order to precisely identify and measure both distinct and obscure peak positions and extrapolate their FWHM. The PL spectrum in Fig. 5A exhibits overlapped emission lines which are conspicuous at 416 nm and 439 nm, respectively, while the third peak is a slightly obscure shoulder which is situated at 465 nm. These energy lines are suggested to be due to photo-excited charge recombination. The varying emission intensity and peak position in the luminescence spectrum of CuO nanoparticles have been ascribed to result from the different polarities of the solvent and dielectric constant [17]. However, in present study, the different PL emission intensities and peak positions may be induced by the different size distributions of the $CuSO_4$ NCs as confirmed from the SEM micrographs

Table 1 Results of elemental quantification on the sample displaying weight percentage composition of elements obtained from the cross-sectional SEM image shown in Fig. 4A

Spectrum	In stats	C	O	S	Cu	Total
Spectrum 1	Yes	5.04	73.36	10.12	11.49	100
Spectrum 2	Yes	5.58	69.93	10.22	14.28	100
Spectrum 3	Yes	6.7	54.6	13.24	25.47	100
Spectrum 4	Yes	6.4	54.3	13.62	25.67	100
Spectrum 5	Yes	4.59	51.52	12.38	31.51	100
Mean		5.66	60.74	11.92	21.68	100
Std. deviation		0.89	10.1	1.66	8.45	
Max		6.7	73.36	13.62	31.51	
Min		4.59	51.52	10.12	11.49	

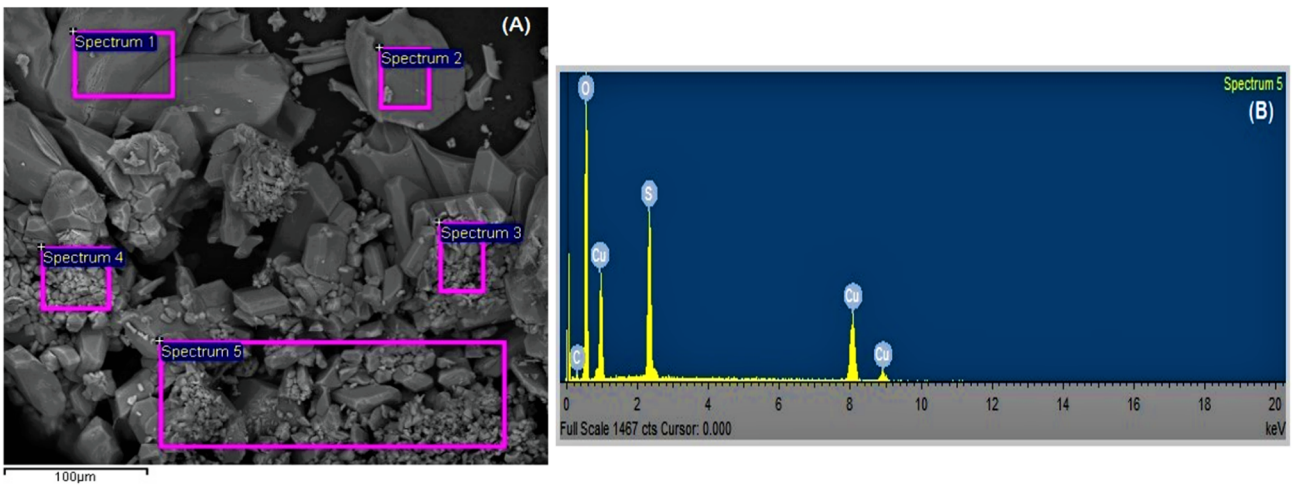

Fig. 4 **A** Cross-sectional SEM micrograph of $CuSO_4$ nanocrystals on FTO-glass indicating selected area of EDX spectrum analysis. **B** EDS spectrum

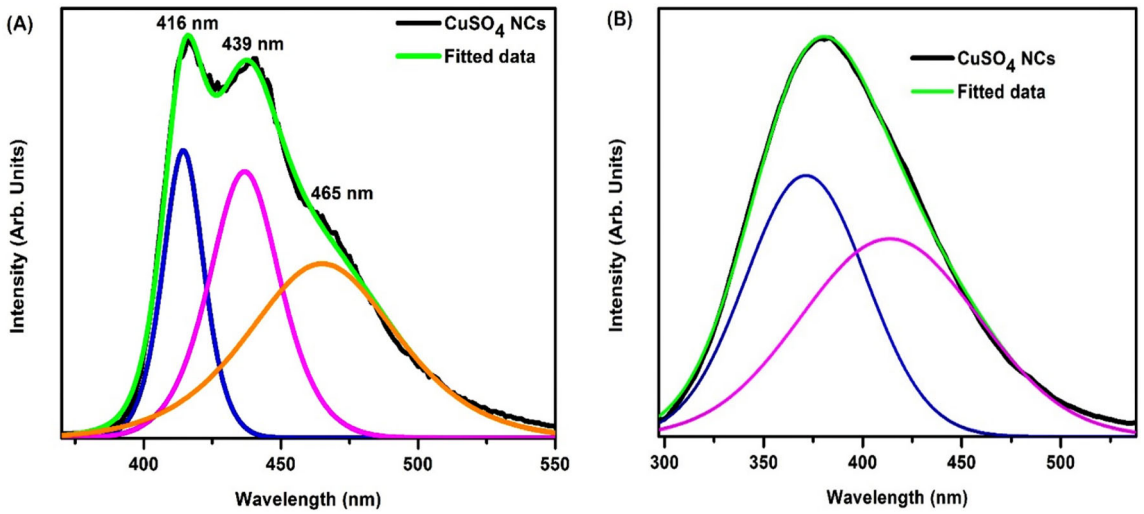

Fig. 5 Room-temperature **A** Photoluminescence spectroscopy and **B** Fluorescence spectroscopy measurements obtained from the $CuSO_4$ NCs

and, hence, can trigger some modifications in the optical properties of the material. This phenomenon can further be described in a case of weak confinement which gives rise to a red-shift in the emission line as the size of the crystal increases.

The FL spectrum from $CuSO_4$ NCs exhibits an emission band at a central wavelength of 380 nm with a FWHM value of 94 nm as shown in Fig. 5B. Results obtained after the application of appropriate deconvolution procedure and fit functions to the FL spectrum data indicate that the broad peak with central wavelength peak at 380 nm is a contribution due to overlapped spectral bands with wavelength peaks at 375 and 425 nm, respectively, as shown in Fig. 5B. The FL spectrum of a solution of graphene quantum dots (QDs) and 10 mM $CuSO_4$ was reported to emit a low-intensity FL at 440 nm [18–21]. Also, the effect of concentration of copper sulphate on graphene QDs FL has been reported to give rise to a decrease in the intensity of graphene QDs FL up to the time a constant state value is attained [22].

In order to precisely identify the compounds/materials specifically by their functional groups, a PerkinElmer Spectrum Two FT-IR Spectrometer in the 400–4000 cm^{-1} spectral range was used with potassium bromide (KBr) as the beam-splitter material. The different bands and their respective transmissions which were observed from the $CuSO_4$ NCs are displayed in the FT-IR spectrum as shown in Fig. 6. A total number of 5 characteristic peaks at the band values of 610, 868, 1074, 1668, and 3123 cm^{-1} were conspicuous in the FT-IR spectrum. The stretching frequency at 3123 cm^{-1} can be assigned to the O–H stretching vibrations of water [v (H_20)]. Similarly, the band with medium intensities at 1668 cm^{-1} and 868 $cm^{-1}$is both ascribed as the bending vibrations and rocking modes of water [$v_2(H_2O)$ and $v_R(H_2O)$], respectively, while the strong bands at 1074 and 610 cm^{-1} are the stretching and bending vibrations of sulphate ion [$v_3(SO_4)^{2-}$ and $v_4(SO_4)^{2-}$], respectively. The vibration modes obtained from present study for cupric sulphate crystals are in correspondence with other reported infrared data on similar compounds [23–28]. However, it is assumed tentatively that the slight variation in some peak positions as observed from Fig. 6 compared to other data might be introduced as a result of modifications in the magnitude of bond interactions/binding strength between the water molecules and the sulphate ions.

The absorption spectrum of $CuSO_4$ NCs shown in Fig. 7A was acquired at room temperature using a PerkinElmer Lambda 365 Double Beam UV–Visible Spectrophotometer (in the range 300–1000 nm) with the aid of a variable angle transmission accessory which allows reproducible measurement at several angles without necessarily moving the mounted sample. To complement the absorbance measurements acquired in Fig. 7A by extending the investigation from visible range towards higher wavelengths in the near infrared region (from 400 to 2500 nm as shown in Fig. 7B), additional analysis on the absorbance of $CuSO_4$ NCs was carried out using a

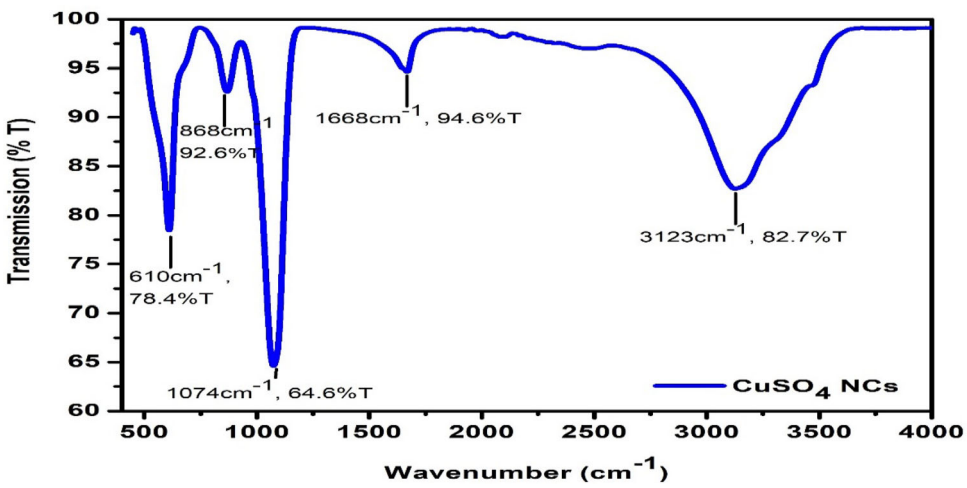

Fig. 6 FT-IR Spectrum of $CuSO_4$ NCs

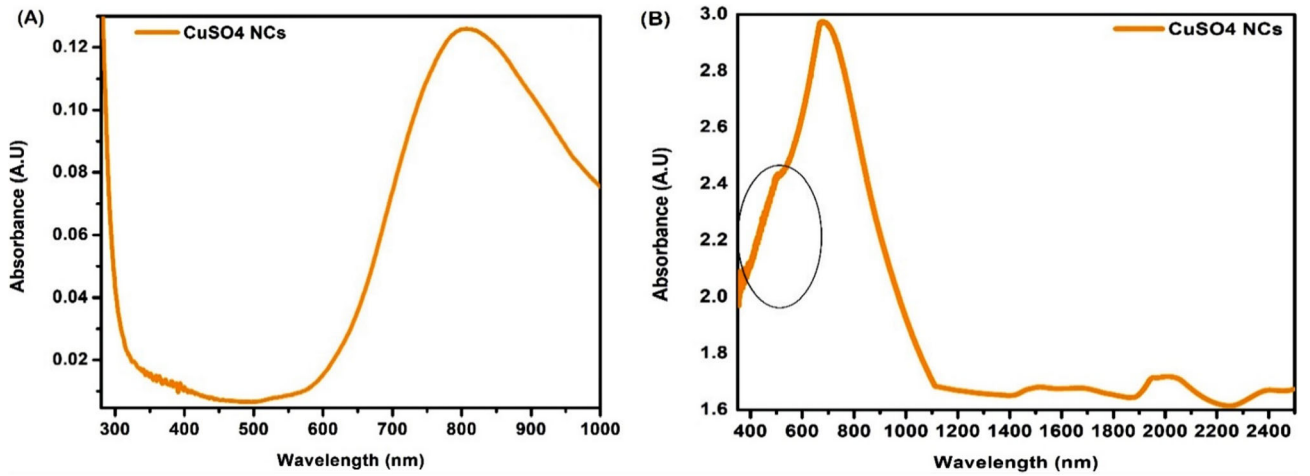

Fig. 7 **A** UV–VIS absorption spectrum of $CuSO_4$ NCs dissolved in deionized water **B** UV–VIS–NIR absorption spectra of $CuSO_4$ NCs on FTO

Bruker Vertex 80v spectrometer equipped with an externally connected air-cooled deuterium lamp as UV source. The absorption spectrum collected using the Bruker Vertex 80v spectrometer is displayed in Fig. 7B. The limit of the detector used in acquiring the UV–VIS–NIR spectrum in Fig. 7B falls within the region enclosed in a circle as depicted in the absorption spectrum. In Fig. 7A, a broad absorption spectrum from 690 to 1100 nm, having a FWHM value of 254 nm and an energy excitonic absorption peak in the visible region at 810 nm was observed for a solution containing $CuSO_4$ NCs dissolved in water. The broad absorption band in the 1.14 to 1.79 eV region originates from the $d \rightarrow d$ transitions of copper ions (Cu^{2+}) [29]. The absorption peak at 810 nm observed in present work corresponds to the value of wavenumber reported as the absorption band maximum for $Cu(H_2O)_6{}^{2+}$ ion in H_2O [30], although it varies from the value of 780 nm which was reported as the absorption band of copper sulphate ($CuSO_4$) in $H_2{}^{16}O$ solution [31]. Furthermore, different absorption peaks at 230 nm and 810 nm have been reported in a study which involves the investigation of the UV–Visible absorption spectrum of copper sulphate solution in graphene QDs bath at different wavelengths [22]. The peak appearing at 810 nm seems to correspond with present results and can be ascribed to copper sulphate.

In Fig. 7B, the highest absorption peak for $CuSO_4$ NCs on FTO was observed at 678 nm contrary to the value that was obtained when it is dissolved in water as described in Fig. 7A. The absorption peak value of 678 nm is closely related to what was reported as the absorption peak centre for Cu@$CuSO_4$ [32]. Likewise,

the FWHM value of 390 nm deduced from the absorption spectrum in Fig. 7B is significantly higher than the value of 254 nm obtained for $CuSO_4$ in water solution. Increase in absorption intensities in annealed $CuSO_4$ shell has been described to be associated with deep levels linked with the sulphur vacancies or foreign defects in addition to extreme excitonic emission of $CuSO_4$ shell [32]. The crystal size of $CuSO_4$ is expected to become smaller in water due to its solubility which can account for the reduction in measured FWHM value. Similarly, the polarity of water and its dielectric constant are suggested to induce a shift in the observed absorption peak of $CuSO_4$ NCs in the present study. The broad absorption band, along with the distinct extensive FWHM value in present study, is an indication that the synthesized $CuSO_4$ nanocrystals have non-uniform size distribution. During an investigation of the effect of shock waves on copper sulphate crystals [33], high values of FWHM obtained from the optical transmission spectrum of the crystals were reported to be favourable for transmitter and filter applications at specific wavelength regions.

To further investigate the vibrational modes and strain characteristics of the $CuSO_4$ NCs, room-temperature Raman spectroscopy measurements from 20 to 3750 cm^{-1} were conducted on the sample while the spectrum measured from the Raman scattering corresponding to the crystals is displayed in Fig. 8A. An elaborate description of the Raman instrument specification and parameters adopted during spectral acquisition has been reported elsewhere [34]. For clarity, the vibrational modes at lower frequencies (50 cm^{-1} to 1750 cm^{-1}) are displayed more clearly with their respective Raman peaks as indicated in Fig. 8B. A total number of 16 vibrational frequencies were observed from Raman scattering unlike in FT-IR with only 5 active modes. The observed Raman at 82 cm^{-1}, 125 cm^{-1}, 200 cm^{-1}, 241 cm^{-1}, 274 cm^{-1}, 329 cm^{-1}, 450 cm^{-1}, 610 cm^{-1}, 714 cm^{-1}, 870 cm^{-1}, 984 cm^{-1}, 1056 cm^{-1}, 1094 cm^{-1}, 1140 cm^{-1}, 1650 cm^{-1}, and a broad band from 3000 to 3500 cm^{-1} with centre approximately at 3240 cm^{-1}. The low frequency at 82 cm^{-1} in present study is associated with the translational modes of the sulphate ions [$T(SO_4)^{2-}$] [25]. However, the vibrational frequency at 82 cm^{-1} (although slightly shifted to 83.5 cm^{-1}) has been reported by other authors [35] to result from the rotation of water and sulphate oxygens over the residual water-copper axis. The low frequency line at 125 cm^{-1} is related to the intermolecular lattice vibration of copper and sulphate ions [36], while frequencies between 200 to 350 cm^{-1} can be ascribed to the bending modes of $Cu(H_2O)_4$ ions. The antisymmetric bending mode at 610 cm^{-1} was also been observed in the FT-IR spectrum and corresponds to the v_4 lattice vibrations of the sulphate ion [v_4 $(SO_4)^{2-}$]. The weak bands at 714 cm^{-1} and 870 cm^{-1} are the librational modes of water molecules which are largely shifted alongside isotropic exchange of hydrogen atoms in accordance with earlier results which has been reported [25, 37]. In Fig. 8, the symmetric stretching mode [v_1 $(SO_4)^{2-}$] of the sulphate ion is observed at 984 cm^{-1} with strong intensity, while the three vibrational frequency bands observed at 1056 cm^{-1}, 1094 cm^{-1}, and 1140 cm^{-1}

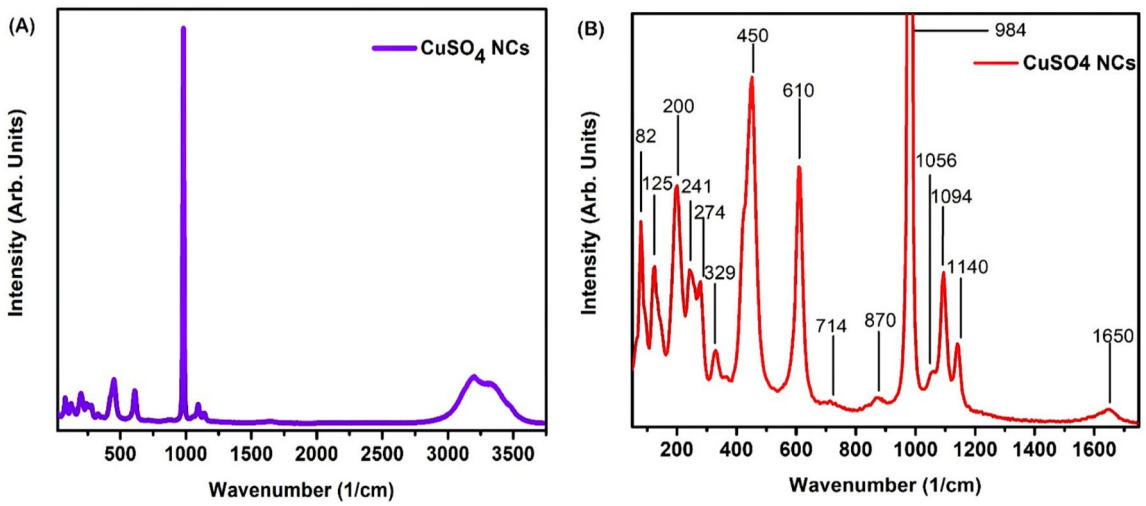

Fig. 8 **A** Room-temperature Raman spectrum of $CuSO_4$ NCs on FTO **B** Zoomed image of **A** showing observed peaks

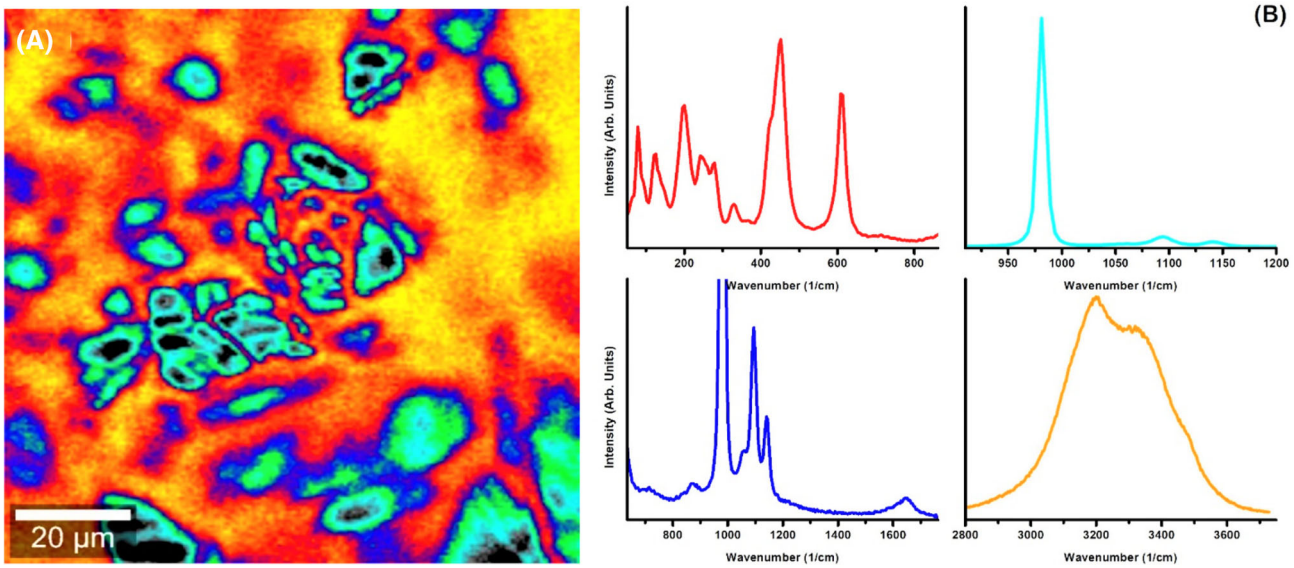

Fig. 9 **A** Colour-mapped Raman image of $CuSO_4$ NCs obtained from large-area scan of the sample **B** Corresponding colour-mapped Raman spectra from **A** showing relative line intensities that are more visible

can be ascribed to the antisymmetric stretching mode v_3 of the free sulphate ions [v_3 $(SO_4)^{2-}$]. The frequency band with weak intensity at 1650 cm^{-1} and the broad frequency line with medium intensity between 3000 and 3400 cm^{-1} are assigned to the water molecules [v_2 (H_2O)] and [$v_1 + v_3$ (H_2O)] in the crystals, respectively.

A large-area colour-mapped Raman image obtained from the NCs is shown in Fig. 9A while the corresponding colour-mapped Raman spectra for the displayed Raman image in Fig. 9A are displayed in Fig. 9B. It is important to note that the full-wavenumber colour-mapped Raman spectra for each spectrum in Fig. 9B are identical but only differ in intensities specifically at the wavenumber regions displayed in the Raman spectra, respectively, with these regions having stronger Raman intensity compared to the rest of the wavenumber regions. The change in Raman intensities at specific regions on the colour-mapped image can tentatively be suggested to be due to phase differences which can be induced by variation in thickness and strain at different regions on the deposited layer.

4 Conclusion

In summary, an investigation of the optical and structural properties of cupric sulphate NCs which was developed using hydrothermal methods has been reported. The results obtained from AFM analysis of the sample revealed corrugated surface morphology characterized by densely populated nanosized crystal-shaped particles, with an average height of 65 nm, and a lateral size dimension in the range 90–450 nm which corresponds to a mean base length of 270 nm for the crystal-like structures, as determined from height profile measurements. Further studies conducted on the as-grown sample show a high surface roughness value of 21 nm root-mean square (RMS) for a scan size of 5 × 5 μm^2, with a threshold height of ~ 103 nm projecting from the surface. Room-temperature PL measurements on the NCs reveal overlapped emission lines which are conspicuous at 416 nm and 439 nm, respectively, while the third peak is a slightly obscure shoulder which is situated at 465 nm. These energy lines are suggested to be due to photo-excited charge recombination. Also, the FL spectrum from $CuSO_4$ NCs exhibits a broad emission at 380 nm which was resolved by the application of appropriate deconvolution procedure and fit functions as contributions from overlapped spectral bands with wavelength peaks at 375 and 425 nm, while a total number of 16 vibrational frequencies were observed from Raman scattering and 5 active modes has been observed in the Fourier Transform Infrared (FT-IR) spectrum. The results contained in the present study can be useful towards the advancement of innovative procedures for controlling the quality of crystal deposition with

the aim of enhancing their structural integrity and optical properties.

Acknowledgements

This work is based on the research supported wholly/in part by the National Research Foundation of South Africa (Grant Numbers: 138532, and 150863), and Govan Mbeki Research & Development Centre (GMRDC) at the University of Fort Hare.

Author contributions

CCA: Investigation, Conceptualization, Visualization, Writing—Original draft. ELM: Conceptualization, Project administration, Resources, Supervision, Validation.

Funding

Open access funding provided by University of Fort Hare. Funding was provided by Govan Mbeki Research and Development Centre, University of Fort Hare, South African National Research Foundation (138532).

Data availability

The authors wish to confirm that data sharing is not applicable to this article as no new data were created or analysed in this study.

Declarations

Competing interests The authors wish to confirm that there are no known conflicts or competing interests associated with this publication, and there have been no personal or financial interests related to this work that could have influenced its outcome.

Ethical approval The authors confirm that this manuscript complies with the journal's standards and instructions to authors on notation, significant figures, experimental errors and the use of the Scherrer equation.

References

1. F.J. Justel, D.M. Camacho, M.E. Taboada, K.J. Roberts, Crystallization of copper sulphate pentahydrate from aqueous solution in absence and presence of sodium chloride. J. Cryst. Growth **525**, 125204 (2019)
2. M. Mary Anne, M. Daniel Sweetlin, Synthesis and characterization of pure and L-proline doped copper sulphate single crystals. J. Mater. Sci. Mater. Electron. **34**, 974 (2023)
3. N.A. Bakr, T.A. Al-Dhahir, S.B. Mohammad, Growth of copper sulfate pentahydrate single crystals by slow evaporation technique. J. Adv. Phys. **13**(2), 4651–4656 (2017)
4. V.L. Manomenova, M.N. Stepnova, V.V. Grebenev, E.B. Rudneva, A.E. Voloshin, Growth of $CuSO_4 \cdot 5H_2O$ single crystals and study of some of their properties. Cryst. Growth **58**(3), 505–509 (2013)
5. S. Höfer, J. Popp, T.G. Mayerhöfer, Determination of the dielectric tensor function of triclinic $CuSO_4{\cdot}5H_2O$. Vib. Spectrosc. **67**, 44–54 (2013)
6. M. Kacmar, M. Orendac, J. Cernak, A. Feher, The experimental study of the magnetic field dependence of specific heat in S=1/2 quantum spin chain $CuSO_4$. $5H_2O$. J. Magn. Magn. Mater. **196–197**, 430–432 (1999)
7. W.G. Bos, T.O. Klaassen, N.J. Poulis, Indirect nuclear spin-spin interaction in $CuSO_4$. $5H_20$. Physica B+C **125**(3), 269–278 (1984)
8. R.D. Brittain, K.H. Lau, D.L. Hildenbrand, Effusion studies of the decomposition of $CuSO_4$ and $CuO.CuSO_4$. J. Phys. Chem. **93**, 5316–5319 (1989)
9. L. Mentar, A study of the electrodeposition of Co–Cu alloys thin films on FTO substrate. Ionics **18**, 223–229 (2012)

10. C. Sabitha, K. Deva Arun Kumar, S. Valanarasu, A. Saranya, I. Hubert Joe, Cu:ZnS and Al:ZnS thin films prepared on FTO substrate by nebulized spray pyrolysis technique. J. Mater. Sci. **29**, 4612–4623 (2018)
11. S. Zhang, J. Yan, S. Yang, Xu. Yuehua, X. Cai, X. Li, X. Zhang, F. Peng, Y. Fang, Electrodeposition of Cu_2O/g-C_3N_4 heterojunction film on an FTO substrate for enhancing visible light photoelectrochemical water splitting. Chin. J. Catal. **38**, 365–371 (2017)
12. W. Martens, R.L. Frost, J.T. Kloprogge, P.A. Williams, Raman spectroscopic study of the basic copper sulphates: implications for copper corrosion and 'bronze disease.' J. Raman Spectrosc. **34**, 145–151 (2003)
13. C.C. Ahia, N. Tile, E.L. Meyer, J.R. Botha, Crystallinity and morphology of InSb epitaxial layers grown on GaSb by MOVPE using TDMASb and TMSb as Sb precursors. Mater. Sci. Semicond. Process. **127**, 105698 (2021)
14. S. Santos, V. Barcons, H.K. Christenson, J. Font, N.H. Thomson, The intrinsic resolution limit in the atomic force microscope: implications for heights of nano-scale features. PLoS ONE **6**(8), e23821 (2011)
15. Y. Maruyama, T. Ebihara, H. Nishiyama, Y. Konyuba, M. Senda et al., Direct observation of protein microcrystals in crystallization buffer by atmospheric scanning electron microscopy. Int. J. Mol. Sci. **13**(8), 10553–10567 (2012)
16. J.W. Mullin, *Crystallization* (Butterworth-Heinemann, Oxford, 2001)
17. N.C. Horti, M.D. Kamatagi, S K. Nataraj, Photoluminescence properties of copper oxide nanoparticles: effect of solvents, in *Prof. Dinesh Varshney Memorial National Conference on Physics and Chemistry of Materials* (Indore, India, 2019).
18. X. Liu, W. Gao, X. Zhou, Y. Maa, Pristine graphene quantum dots for detection of copper ions. J. Mater. Res. **29**(13), 1401–1407 (2014)
19. K. Habiba, V.I. Makarov, J. Avalos, M.J.F. Guinel, B.R. Weiner, G. Morell, Luminescent graphene quantum dots fabricated by pulsed laser synthesis. Carbon **64**, 341–350 (2013)
20. X. Fang, M. Li, K. Guo, J. Li, M. Pan, L. Bai, M. Luoshan, X. Zhao, Graphene quantum dots optimization of dye-sensitized solar cells. Electrochim. Acta **137**, 634–638 (2014)
21. M. Roding, S.J. Bradley, M. Nyden, T. Nann, Fluorescence lifetime analysis of graphene quantum dots. J. Phys. Chem. C **118**(51), 30282–30290 (2014)
22. Z. Protich, K.S.V. Santhanam, A. Jaikumar, S.G. Kandlikar, P. Wong, Electrochemical deposition of copper in graphene quantum dot bath: pool boiling enhancement. J. Electrochem. Soc. **163**(6), E166–E172 (2016)
23. I. Gamo, Infrared absorption spectra of water of crystallization in copper sulfate penta- and monohydrate crystals. Bull. Chem. Soc. Jpn. **34**(6), 764–766 (1961)
24. J. Fujita, K. Nakamoto, M. Kobayashi, Infrared spectra of metallic complexes. II. The absorption bands of coordinated water in aquo complexes. J. Am. Chem. Soc. **78**(16), 3963–3965 (1956)
25. J. Berger, Infrared and Raman spectra of $CuSO_4$, $5H_2O$; $CuSO_4$, $5D_2O$; and $CUSeO_4$, $5H_2O$. J. Raman Spectrosc. **5**(2), 103–114 (1976)
26. E. Moroydor Derun, N. Tugrul, F.T. Senberber, A.S. Kipcak, S. Piskin, The optimization of copper sulfate and tincalconite molar ratios on the hydrothermal synthesis of copper borates. Int. J. Chem. Mol. Eng. **8**(10), 1152–1156 (2014)
27. C.M. Bhambere, N.G. Durge, Study on structural, spectral, and optical properties of copper sulphate doped L-methionine crystal. J. Emerg. Technol. Innov. Res. **8**(7), b776–b779 (2021)
28. H.W. Garba, K. Abubakar, M.S. Abdullahi, R. Watanpal, Synthesis, spectroscopy study of copper (II) sulphate pentahydrate, tetra-amminocopper (II) sulphate and bis-ethylenediamine copper (II) sulphate in the catalytic reduction of nitrophenol derivatives. Int. J. Sci. Eng. Sci. **4**(10), 19–26 (2020)
29. V.S. Kishan Kumar, B.S.V.S.R. Acharyulu, S.B.S. Sastry, Absorption, emission, and thermoluminescence of copper doped alkali sulphate phosphors. Phys. Stat. Sol. (B) **175**, 287–297 (1993)
30. J. Halpern, A.C. Harkness, Spectra of some transition metal ions and complexes in D_2O. J. Chem. Phys. **31**, 1147 (1959)
31. G. Jancso, Effect of D and 18O isotope substitution on the absorption spectra of aqueous copper sulfate solutions. Radiat. Phys. Chem. **74**, 168–171 (2005)
32. Z. Zarghami, M. Ramezani, M. Maddahfar, Simple microwave-assisted synthesis of Cu@$CuSO_4$ as co-catalyst of TiO_2 for photocatalytic degradation of methylene blue. Mater. Lett. **152**, 21–24 (2015)
33. A. Sivakumar, M. Sarumathi, S.S.J. Dhas, S.A.M.B. Dhas, Enhancement of the optical properties of copper sulfate crystal by the influence of shock waves. J. Mater. Res. **35**(4), 391–400 (2020)
34. C.C. Ahia, N. Tile, E.L. Meyer, J.R. Botha, Effect of InSb deposition time on low-temperature photoluminescence and room temperature Raman of MOVPE grown InSb/GaSb nanostructures. Physica E **123**, 114197 (2020)
35. M.T. Ruggiero, T.M. Korter, Uncovering the terahertz spectrum of copper sulfate pentahydrate. J. Phys. Chem. A **120**(2), 227–232 (2016)
36. X. Fu, G. Yang, J. Sun, J. Zhou, Vibrational spectra of copper sulfate hydrates investigated with low-temperature Raman

spectroscopy and terahertz time domain spectroscopy. J. Phys. Chem. A **116**(27), 7314–7318 (2012)
37. I. Nakagawa, T. Shimanouchi, Infrared absorption spectra of aquo complexes and the nature of coordination bonds. Spectrochim. Acta **20**, 429–439 (1964)